

Molecular dynamics simulation of the behavior of typical radiation defects under stress gradient field in tungsten

Cite as: J. Appl. Phys. **130**, 125103 (2021); <https://doi.org/10.1063/5.0059748>

Submitted: 11 June 2021 • Accepted: 08 September 2021 • Published Online: 24 September 2021

 Jingzhong Fang, Lixia Liu, Ning Gao, et al.



View Online



Export Citation



CrossMark

ARTICLES YOU MAY BE INTERESTED IN

Atomistic simulation of nanoindentation response of dual-phase nanocrystalline CoCrFeMnNi high-entropy alloy

Journal of Applied Physics **130**, 125102 (2021); <https://doi.org/10.1063/5.0057591>

Molecular dynamics simulations of inelastic x-ray scattering from shocked copper

Journal of Applied Physics **130**, 125901 (2021); <https://doi.org/10.1063/5.0057044>

Extremely thin reflective metasurface for low-frequency underwater acoustic waves: Sharp focusing, self-bending, and carpet cloaking

Journal of Applied Physics **130**, 125304 (2021); <https://doi.org/10.1063/5.0041092>

Journal of Applied Physics **Special Topics** Open for Submissions

Learn More



Molecular dynamics simulation of the behavior of typical radiation defects under stress gradient field in tungsten

Cite as: J. Appl. Phys. **130**, 125103 (2021); doi: [10.1063/5.0059748](https://doi.org/10.1063/5.0059748)

Submitted: 11 June 2021 · Accepted: 8 September 2021 ·

Published Online: 24 September 2021



Jingzhong Fang,¹ , Lixia Liu,² Ning Gao,^{3,4,a)} Wangyu Hu,² and Huiqiu Deng^{1,a)}

AFFILIATIONS

¹School of Physics and Electronics, Hunan University, Changsha 410082, China

²College of Materials Science and Engineering, Hunan University, Changsha 410082, China

³Institute of Frontier and Interdisciplinary Science and Key Laboratory of Particle Physics and Particle Irradiation (MOE), Shandong University, Qingdao 266237, China

⁴Institute of Modern Physics, Chinese Academy of Sciences, Lanzhou 730000, China

^{a)}Authors to whom correspondence should be addressed: ning.gao@sdu.edu.cn and hq Deng@hnu.edu.cn

ABSTRACT

In the fusion environment, a complex stress field is generated in materials, which affects the evolution of radiation defects. In this study, the behaviors of radiation-induced defects under the effect of stress gradient field in tungsten are carefully simulated at the atomic scale with the molecular dynamics (MD) method. It was found that the stress gradient field affects the migration properties of interstitial defects, resulting in the energy barriers changing with the stress and stress gradient. In the axial stress gradient field, the movement of the 1/2 <111> interstitial dislocation loop is significantly accelerated, and it tends to move toward the region where the stress is concentrated. Within the time scale of the classical MD simulation, the stress gradient has little effect on the migration of vacancies. These results suggested that the stress gradient would cause interstitial defects to accumulate to the region where the stress is concentrated, thereby significantly changing the properties of the tungsten materials.

Published under an exclusive license by AIP Publishing. <https://doi.org/10.1063/5.0059748>

I. INTRODUCTION

In fusion reactors, plasma-facing materials (PFMs) withstand particles and heat loads from the plasma and neutron implantation during reactor operation. Neutron irradiation in materials causes the accumulation of radiation-induced defects in the materials, resulting in significant modification of their crystal structures and properties.^{1–3} In addition to the radiation defects, the PFMs are exposed to high heat flux induced by the fast neutrons and H/He plasma. With the heavy thermal load, complex stress states are built and distributed in the material under fusion conditions. In You *et al.*'s research,⁴ the misfit stress in the regions near bond interfaces induced by the difference in the coefficient of thermal expansion⁵ and thermal stress induced by the temperature gradient⁶ were considered the main source of stresses. According to You *et al.*'s analysis, the internal stress state of the material is related to the material thickness, temperature difference, and other factors.

Because these factors vary in different positions of the material, the local stress of the material also changes accordingly, thus the stress gradient appears in the material.

As potential PFMs in future, fusion reactors, tungsten (W), and W-based alloys have advantages such as high melting point, high thermal conductivity, and low sputtering rate.^{7–9} The defect behavior in W under normal conditions has been extensively studied in experiments,¹⁰ first-principle calculations,^{11–14} and classical molecular dynamics (MD) simulations.^{11,15–17} Wang *et al.*¹⁸ used the MD method to study the defects under stress fields and found that defect fraction in a cluster and the average size of the defect cluster induced by cascade can be affected by the strain. Kirsanov *et al.*¹⁹ studied self and impurity interstitial Al atom migration in both unstressed and stress gradient fields in α -Fe by a computer simulation method. The results indicated that the stress gradient changes the barrier of interstitial migration. In an investigation of dislocation instability in a stress

gradient field in Al, Li *et al.*²⁰ reported that when an initially straight dislocation line is driven by stress whose magnitude increases toward the dislocation motion, the vibrational modes of the dislocation line with wavelength above a threshold value become linearly unstable.

In our previous work,^{21,22} the properties of basic W defects in the equilibrium field were investigated in detail. We have also investigated the effect of temperature gradient fields on the properties of W defects.²³ Based on these studies and the relevance as stated above, from both experimental and engineering viewpoints, we believe that investigating defect nature in the stress gradient field is crucial. Thus, in this study, molecular statics (MS) and MD simulations are employed to investigate defect behaviors in the stress gradient field in W at the atomic scale. Owing to the complexity of simulation conditions and the limitations of simulation methods, first, we will focus on the stress gradient field in a simpler way to explore the underlying physics. The stress is set as the axial stress in the z -direction of the box, and the gradient of the stress is along the same direction. For purposes of comparison, the self-interstitial atoms (SIAs), interstitial dislocation loops, and vacancies are all simulated in both the equilibrium state and stress gradient field of W. The rest of this article is organized as follows. The simulation method is provided in Sec. II. Results and discussions are given in Sect. III. Finally, conclusions are drawn in Sec. IV.

II. SIMULATION METHOD

In this study, MD and MS simulations were performed using the large-scale atomic/molecular massively parallel simulator (LAMMPS).²⁴ A recently fitted Finnis–Sinclair potential by our

group was used for W–W interactions.²⁵ Compared with other W potentials,^{11,15–17,26} this potential more accurately describes the basic properties of typical radiation defects and correctly predicts the properties of radiation-induced dislocation loops in W.^{21,27,28} Moreover, the elastic constants are in good agreement with experimental data,^{22,25} which provides reliability and credibility of the stress gradient calculation results. Figure 1 shows a schematic illustration of the simulation cell used for the MD simulations. The crystal orientations in the x -, y - and z -directions were [100], [010] and [001] respectively. Considering the computational efficiency, and the size of the defect was small (radius < 10 Å), the lengths of simulation the cell in the x - and y -directions were set as 95 Å. Since there were fixed layers in the z -direction, which destroyed the periodicity of the box in the z -direction, the z -axis length was set to 250 Å. The simulation box contained 144 000 W atoms when no defects were included. Periodic boundary conditions were employed in the x - and y -directions.

To introduce gradient stress, a same additional force in the same direction ($-z$ -direction) was applied to each W atom during simulation. The force would accumulate along the $-z$ -direction, resulting in a stress gradient after relaxation, as shown in Fig. 1(a). To keep the total momentum of the box in the z -direction at zero, two fixed layers of atoms were put at the top and bottom of the simulation box to provide a counter-force so that the system held stress instead of accelerating. In order to avoid the fluctuation of the system due to the sudden applied force, this force was gradually increased in the modeling process. σ_{zz} is the component of the pressure tensor in the z -direction, which was used to describe the local stress state of the box in this study.

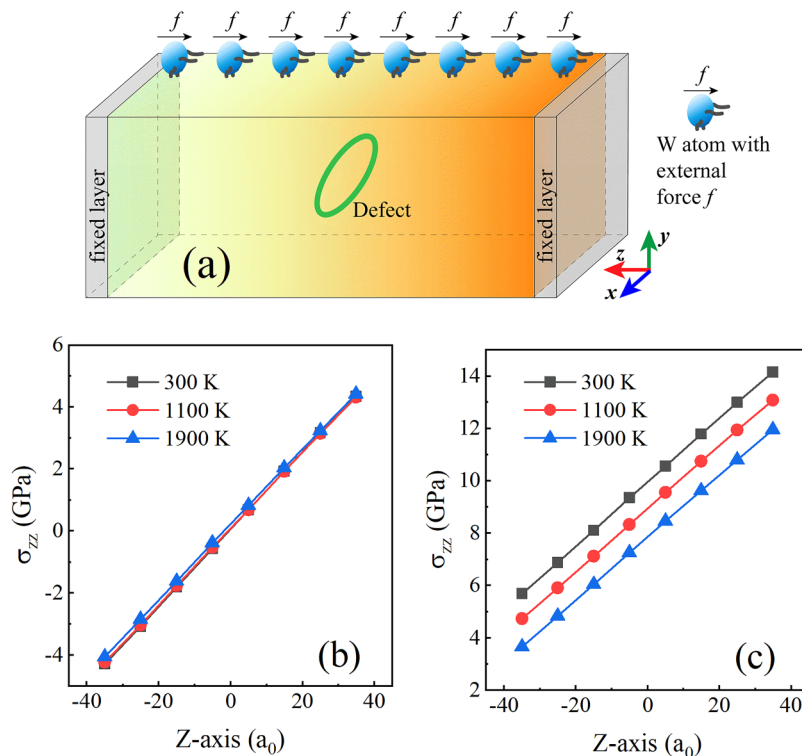


FIG. 1. (a) Schematic diagram of the simulation box in the stress gradient field. An additional force of constant magnitude was applied to each W atom, and a layer of atoms is fixed at the two ends of the box in the z -direction. The radiation defect, e.g., a $1/2 \langle 111 \rangle$ dislocation loop, can be included at the center part of the box. (b) The stress state of the simulation box after relaxation when the force added to each atom is 4×10^{-3} eV/Å. σ_{zz} is the component of the pressure tensor in the z -direction. (c) Stress state of the box after relaxation when an additional strain (-2% , negative sign indicates compressive strain) is applied in the z -direction under condition (b). Due to the different lattice constants at different temperatures, there is a small gap between the three sets of data.

When the force of a single atom was gradually increased to 4×10^{-3} eV/Å, the stress gradient state of the box would be built after sufficient relaxation [Fig. 1(b)]; the box was approximately in the stress range of -4.0 to 4.0 GPa; thus, the stress gradient could be calculated as approximately 0.03 GPa/Å. The temperature had a slight effect [Fig. 1(b)]. In addition, keeping the same stress gradient but a different stress range was considered, which was achieved by applying a given strain along the z -direction of the simulation box. As shown in Fig. 1(c), when the box strain was -2% (negative sign indicates compressive strain), the stress gradient was unchanged, whereas the stress range increased compared with the value in Fig. 1(b). The strain applied to the box is defined as

$$\varepsilon = \frac{L - L_0}{L_0}, \quad (1)$$

where L is the length of the simulation box in the z -direction after deformation and L_0 is the initial length. Through the above methods, different stress gradients and stress ranges could be obtained. In Sec. III, we will indicate the detailed stress state of the box corresponding to each result, e.g., -4.0 to 4.0 GPa at 0.03 GPa/Å. For convenience, the sign convention of the quantities was clarified as follows: the force applied to produce the stress gradient was in the $-z$ -direction; the positive strain meant to stretch the box and the negative strain meant to compress the box; the positive value of σ_{zz} meant a compression state and a negative value meant a tension state; and the movement of the defect in the $+z$ -direction was called a positive movement and vice versa. In particular, we call the box all in a compressive stress state as a compressive stress gradient and vice versa as a tensile stress gradient.

After establishing a stable stress gradient field in different stress ranges, defects were introduced inside the box and fully relaxed before simulations. The relaxation of this system was performed in a constant temperature and volume ensemble (NVT), and the simulation temperature range was 300 – 2500 K. The analysis of the energy and kinetic process of defects in stress gradient with different ranges were provided after the full simulations.

To quantitatively study the diffusion properties of defects, the diffusion coefficient (D) was determined using the Einstein relation equation

$$D = \frac{\langle [r(t) - r(0)]^2 \rangle}{2nt}, \quad (2)$$

where $r(t)$ denotes the position of defect centroid at time t , $\langle \dots \rangle$ denotes the averaging over all defects, and n denotes the dimension (equal to 3 in this work). Due to the limitations imposed by the fixed layer in the z -direction (defects should not touch the fixed layer during the simulation), the effective simulation time was from hundreds of picoseconds to several nanoseconds. During the simulation process, the positions of the interstitial atoms were continuously output at a certain time interval (2 – 8 ps), then the centroid of the defect was calculated to get the MSD ($[r_i(t) - r_i(0)]^2$) data. In order to enhance the accuracy of the results, the MSD data were smoothed based on the method of decomposing the single trajectory into a set of shorter independent segments with equal duration.²⁹

III. RESULTS AND DISCUSSION

A. Simulations of SIAs in W bulk

As is well known, SIAs are usually in a form of a dumbbell or crowdion in bcc metal materials. The lowest-energy configuration of a single SIA in W bulk is the $\langle 111 \rangle$ crowdion.^{11,12,22,28–30} In this study, MS simulations were performed to obtain the formation energy value of SIA in W bulk under the axial strain applied in the $[001]$ direction. The strain range in MS simulations was from -3% to 3% , which covered the box strain range in the MD simulations. The formation energy of an SIA is defined as follows:

$$E_F^{SIA} = E_{N+1} - (N+1)E_C, \quad (3)$$

where E_{N+1} is the total energy of the lattice with a SIA at a certain strain ε_z and E_C is the cohesive energy of a single W atom in perfect W bulk at the same strain. In the absence of strain, the formation energy of a single SIA is 9.46 eV, which was close to the DFT result (9.55 eV).¹² As shown in Fig. 2(a), the formation energy of an SIA decreases greatly as the strain increased from negative to positive values. Similarly, as shown in Fig. 2(a), when the box state changed from compression to extension, the stress in the z -direction (σ_{zz}) decreased by approximately 27 GPa, and the formation energy of a SIA also decreased by approximately 2.5 eV. In the study of Wang *et al.*,^{18,31,32,33} the formation energies of point defects dependent on strains presented the same trend as the result of this study.

In this study, when the stress gradient was applied to the system, the strain at different positions along the stress gradient direction was different. The stress and formation energy dependence on strains (Fig. 2) should be available for defects under the stress gradient effect. Thus, in the stress gradient field, the force experienced by an SIA could be related to the change of its formation energy under the strain effect at different positions, which may be described as follows:

$$f_F = -\alpha \frac{dE_F(\varepsilon_z)}{dz}, \quad (4)$$

where α was supposed to be a vector- or tensor-valued function due to the complexity of the actual potential field. Under the influence of this force, the dumbbell might tend to move to an area with lower formation energy.

From the previous literature,^{11,22,29} we know that the migration energy of a dumbbell in W bulk is minute, which makes it easy to migrate. Based on the present calculations, the applied strain could induce the change in the migration barrier, especially when the box was in the tensile strain [Fig. 2(b)]. When the strain gradually changed from compression to tension, the migration energy increased from 0.02 to approximately 0.27 eV, an order of magnitude change. It can be seen from Fig. 2(b) that the migration energy increases greatly when $\varepsilon > 0$ (the corresponding $\sigma_{zz} < 0$), which means that the migration of the SIA will become difficult under the tensile stress gradient. The change in rotation energy was relatively small. The maximum energy change was approximately 0.24 eV, and the energy near the equilibrium state was the lowest, which increased when the box strain deviated from the equilibrium state. Owing to the axial compression of the box in the z -direction,

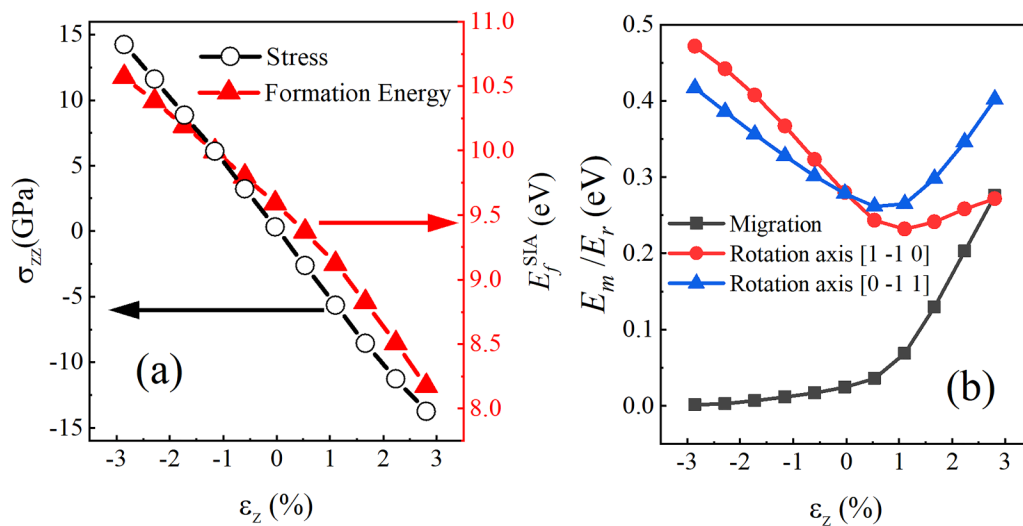


FIG. 2. (a) Formation energies of an SIA at different strains. The black open circles and red solid triangle indicate stress state (σ_{zz}) and formation energy of SIA (E_f^{SIA}), respectively. (b) Migration and rotation energies of an SIA at different strains (with the NEB method³⁴). The migration path is along $\langle 111 \rangle$. The black square indicates migration energies (E_m^{SIA}) of SIA, and the blue triangle and red circle indicate the rotation energies (E_r^{SIA}) around $[011]$ and $[110]$ axes, respectively.

when the dumbbell rotated with $[1\bar{1}0]$ and $[0\bar{1}1]$ as the axes, the rotation energy was slightly different. Following a similar strategy as the last paragraph, we could assume another force due to the stress change related to the change in the dumbbell migration energy under the strain effect at different positions,

$$f_m = -\beta \frac{dE_m(\varepsilon_z)}{dz}, \quad (5)$$

where β was supposed to be a vector- or tensor-valued function. Considering the total influence of the formation and migration energies on the state of a defect in the stress gradient field, we could obtain the additional effect induced by stress gradient on the dumbbell from Eqs. (2) and (3),

$$f = f_F + f_m = -\alpha \frac{dE_F}{dz} - \beta \frac{dE_m}{dz}. \quad (6)$$

Although the values of α and β were expected to have a complicated dependence on temperature and stress and were difficult to determine directly, we could estimate their properties by following the migration behavior in MD simulations.

SIA dumbbell diffusion in bulk BCC metals is known to be preferentially one dimensional in the absence of any applied stress or strain. It can be seen from Fig. 2(b) that in most cases with stress, the rotation energy of the dumbbell is much greater than the migration energy (one-dimensional migration along $\langle 111 \rangle$), which means that the stress will not significantly change dumbbell's one-dimensional motion preference. In MD simulations, the back-and-forth movement of the dumbbell along $\langle 111 \rangle$ dominated its movement during the entire process [Fig. 3(a)]. The position of the $\langle 111 \rangle$ dumbbell randomly changed between state (0) and states (1) and (2). Figure 3(b) depicts the position of the $\langle 111 \rangle$ dumbbell

along the z -direction at different times under the effect of stress gradient (4–12 GPa at 0.03 GPa/Å). Thus, the appearance of the peak and valley in the curve indicated the back-and-forth movement of the dumbbell. Notably, the effect of stress gradient (4–12 GPa at

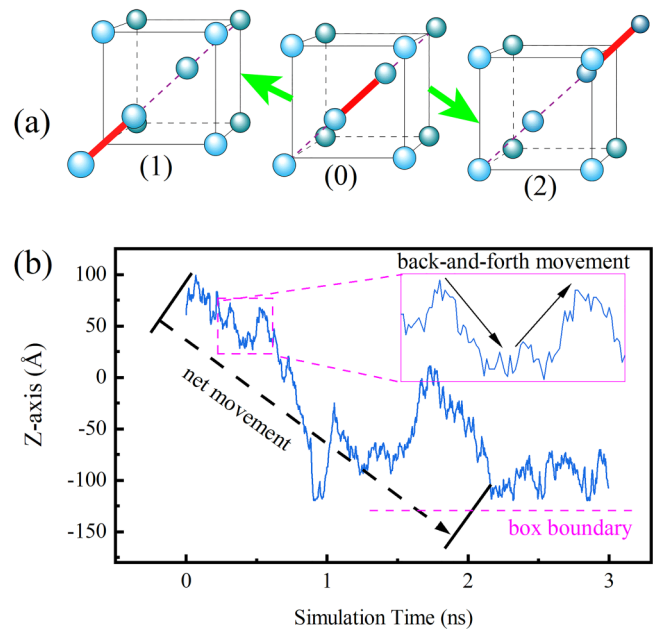


FIG. 3. (a) Schematic diagram of the dumbbell back and forth movement. (b) The movements of a dumbbell in the z -direction in stress gradients at 1100 K, back-and-forth movements in a short time, a net movement in a long time. The dumbbell is initially located at 59.4 Å in the z -direction.

0.03 GPa/Å) resulted in the net movement in a particular direction. for the entire process instead of a totally random diffusion process, i. e., from the low- to the high-stress area in most simulation cases. From this figure, it can also be found a high-temperature results in a strong fluctuation in the defect movement.

The above results clearly showed that the stress gradient did affect the energy and kinetic properties of a defect inside the gradient. Next, we used statistical simulation and analysis to determine the detailed influence of the stress gradient on the direction of movement of the defect. In this respect, we performed the following simulations: (1) A single SIA at stress gradient of about 3.15×10^{-3} GPa/Å with external strain from -1.04% to -0.05% at 500 K. (2) SIAs at the stress gradient of approximately 3.15×10^{-2} GPa/Å with an external strain of -0.7% at 300, 700, 1100 K, respectively. (3) Three SIAs at stress gradient of approximately 3.15×10^{-2} GPa/Å with an external strain of -2.0% at 300, 700, 1100 K, respectively. We used the positive and negative movements to describe the migration direction of defects, “positive” meant the defect moved along the positive z -direction, otherwise, “negative movement” was used, and “uncertain” was used for the uncertain direction. In the first case, the box was in a state of small compressive stress field. A total of 60 simulations were performed using different random initial states. Under such a condition, the ratio of positive to negative movements is about 1:1. When the stress gradient was increased, as did in the second case with a stress gradient of 3.15×10^{-2} GPa/Å, the number of negative movements has been significantly increased [Fig. 4(a)], and the ratio of positive to negative movements reached 16:56. The stresses at both ends of the box were approximately -0.8 and 7.7 GPa, respectively. From this figure, the trend of negative movement of SIAs was the similar at different temperatures. In the third case, the strain of the box increased to -2% while the stress gradient remains the same. From Fig. 4(b), the proportion of negative movement increased and reached 81% of the total. From these three cases, when the stress and stress gradient were small, the net movement of the dumbbell was not obvious, but when the stress and stress gradient increases, the net movement of the dumbbell appeared. In addition, in these three cases, the box was mainly in a state of compressive stress, and the value of compressive stress increased in the negative z -direction. Thus, the above results indicated that in a stress gradient field dominated by compressive stress, SIAs tend to move toward the area of stress concentration.

The results of DFT³⁵ and Chen’s calculations²⁵ showed high binding energies of the interstitial W atoms, which suggested that interstitial clusters were strongly stable. In addition, Chen *et al.* calculated the lowest-energy configuration of interstitial clusters, and the parallel $\langle 111 \rangle$ dumbbell structure was the preferable structure.²⁵ Therefore, in most cases, the SIA and SIA clusters were moving in one dimension and no decomposition occurred. Since the rotation energy of the dumbbell was relatively low, and due to the influence of thermal motion, the rotation of the SIAs might occur during the MD simulation. Figure 5(a) shows the atomic configuration changes of the dumbbell in the rotational movement, from $[111]$ to $[1\bar{1}\bar{1}]$. Using OVITO,³⁶ the trajectory of the dumbbell could be explored [Figs. 5(b)–5(d)]; the blue arrow shows the atom displacement. A single atom moved back and forth along $\langle 111 \rangle$ before and after rotation, which made the trajectory a polygonal line. When the number of interstitials is greater than one, there may be saddle point states during the rotation process of the

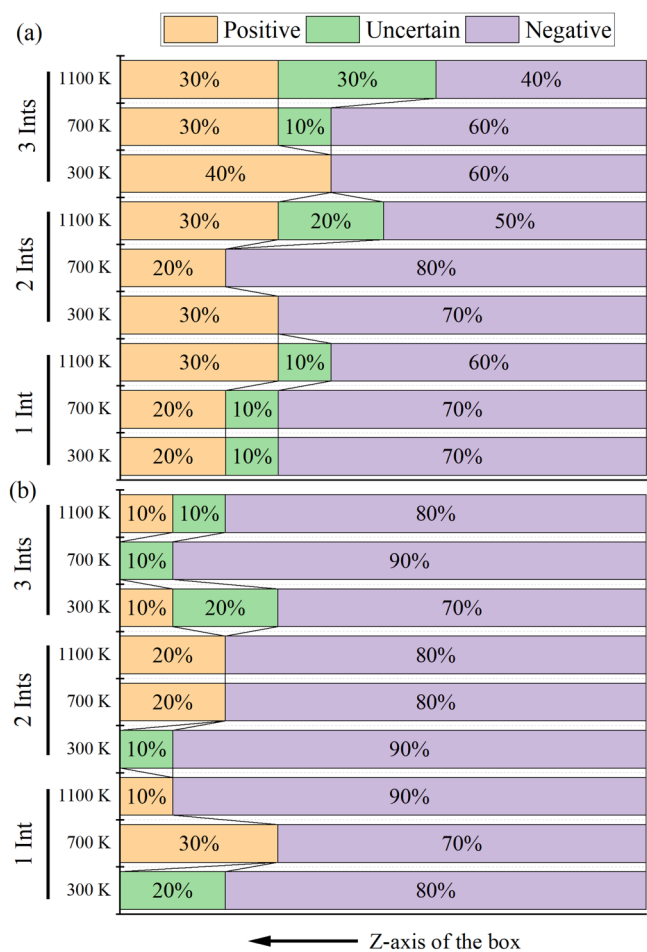


FIG. 4. Migration direction trend statistics of one, two and three SIAs at strain gradient of 3.15×10^{-2} GPa/Å at 300, 700, 1100 K. The purple, yellow, and green bars represent net movement along the $-z$, $+z$ -axis, and uncertain trend, respectively. (a) with an external strain -0.7% (stress range of the box, -0.95 to 7.6 GPa) and (b) with external strain -2.0% (stress range, 6 – 14 GPa).

dumbbell under the stress gradient. As shown in Figs. 5(c) and 5(d), the two SIAs formed an approximately equilateral triangle in a unit cell, and the three SIAs formed an approximately regular tetrahedron. These metastable states would be overcome by thermal fluctuations during a long simulation (i.e., 1.2 – 2.0 ns), resulting in a parallel crowdion cluster again. In previous reports, Zhou *et al.*³⁷ and Wang *et al.*³⁸ conducted detailed studies on the migration and rotation of 1 to 7 SIAs. In Zhou’s research, the energy of the coplanar, non-coplanar, and cross rotation of the two SIAs were 1.52 , 1.31 , and 1.77 eV, respectively. The coplanar and non-coplanar rotations correspond to the “rotation” case in Fig. 5 in this paper, and the cross rotation corresponds to the “trap” case in Fig. 5. The rotation energy of 3-SIA cluster was 1.73 eV in Zhou’s research.

The above-mentioned rotation process could also be observed under normal conditions, but it disappeared as the stress increased.

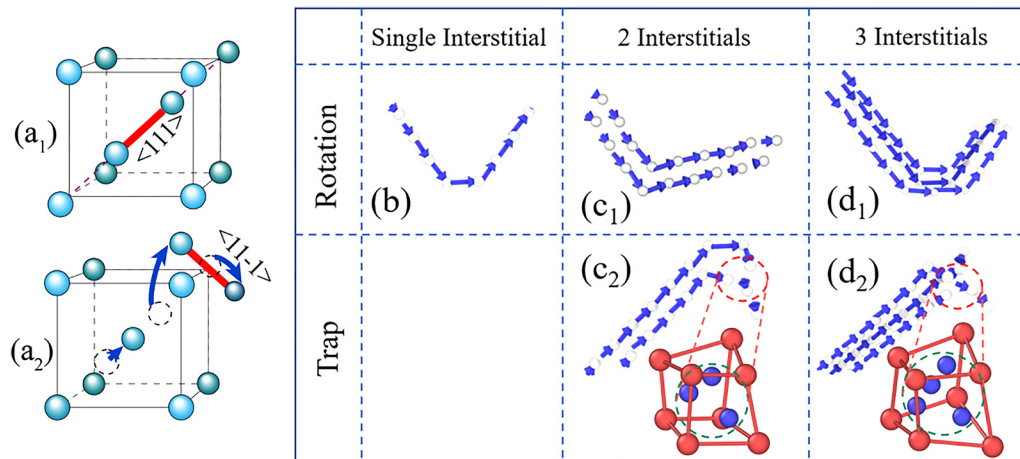


FIG. 5. (a) Rotation of $\langle 111 \rangle$ dumbbell. (b)–(d) The trajectory of one, two, and three SIAs, respectively, when they rotate.

This could be explained by the result shown in Fig. 2(b), when the simulated box was in tension or compression, the rotation energy increased as the stress increased. Figure 6 shows the trajectory of a single dumbbell both in the equilibrium and stress gradient fields. Comparing Figs. 6(a) and 6(b), the rotation in Fig. 6(b) was limited on the left side of the box, the region with lower stress—whereas the rotation in Fig. 6(a) distributed smoothly.

B. Simulations of the $1/2 \langle 111 \rangle$ interstitial loop

In the fusion environment, dislocation loops might be generated in W due to irradiation. Transmission electron microscopy (TEM) studies revealed prismatic dislocation loops with Burgers

vectors $a/2 \langle 111 \rangle$ and $a \langle 100 \rangle$,³⁹ where a is the lattice parameter. In this study, the $a/2 \langle 111 \rangle$ dislocation loops are investigated with MS and MD simulations, since the $a/2 \langle 111 \rangle$ loops dominated the TEM results.³⁹ We applied different strains to the box in the z -direction, under which the system was relaxed for 40 ps at 300 K, followed by energy minimization through MS calculations. Under the effect of different strains, the most obvious change in the loop was that the change in its stable habit plane orientation. Figure 7(a) illustrates the habit plane rotation process of the dislocation loop under a certain stress state. Under stress, the adjacent $\langle 111 \rangle$ crow-dions had a small relative displacement along $\langle 111 \rangle$, resulting in the overall habit plane rotation. In the simulation study of $a/2 \langle 111 \rangle$ dislocation loops in iron by Gao *et al.*,⁴⁰ it was found that

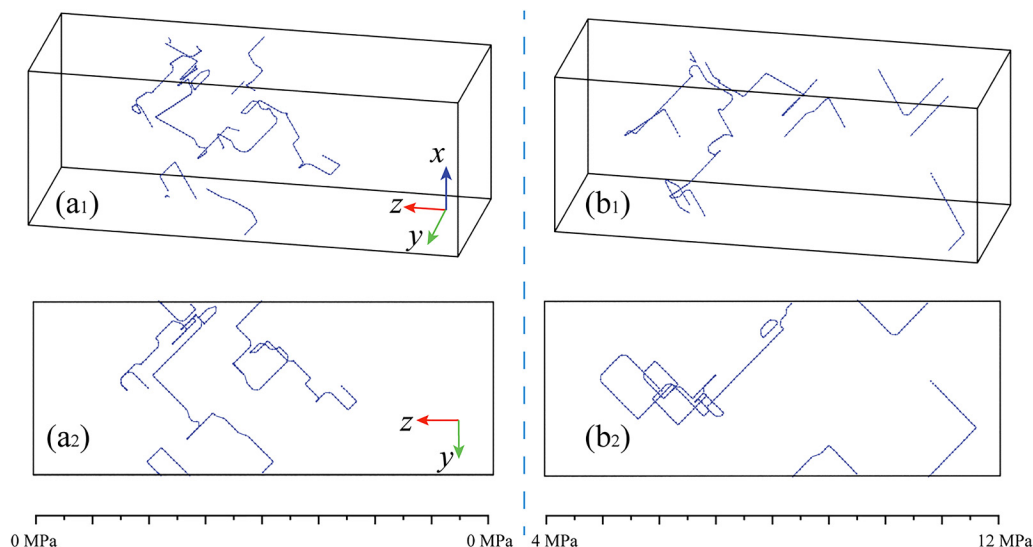


FIG. 6. The trajectory of the dumbbell at 1100 K in (a) equilibrium field and (b) stress gradient field. Inflections of the trajectory (a polyline) mean rotations of the dumbbell.

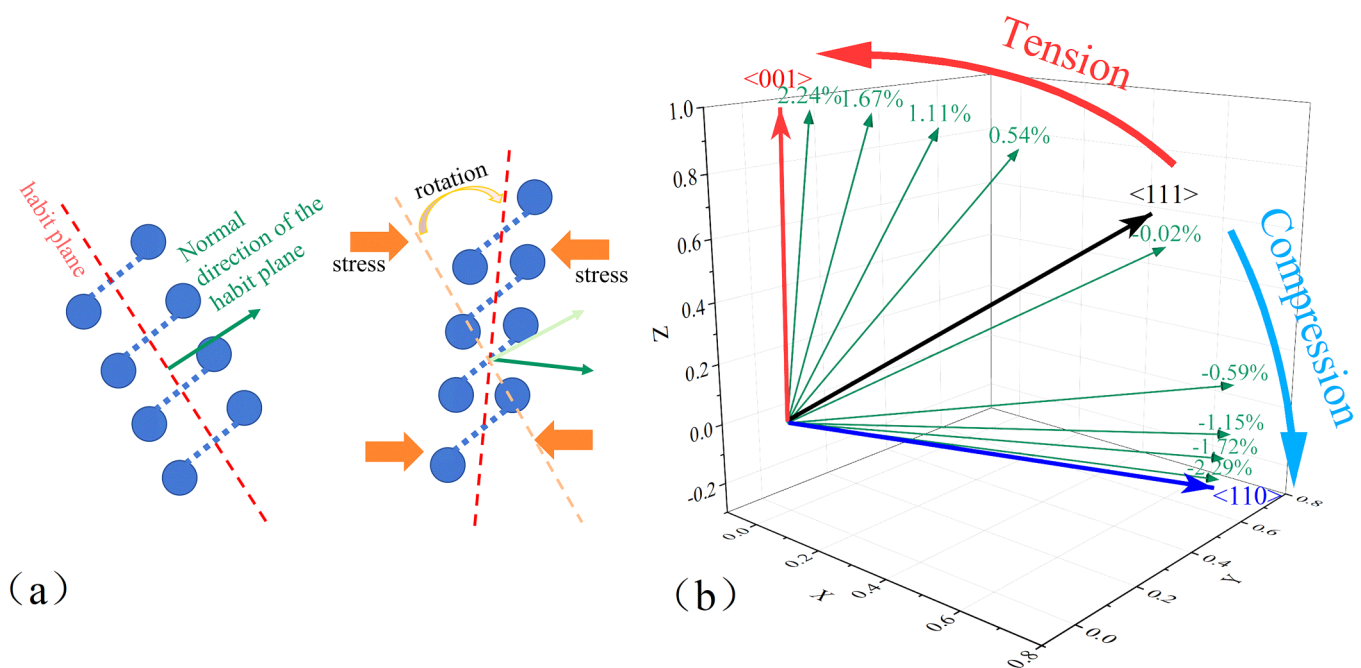


FIG. 7. (a) Schematic diagram of the habit plane rotation of the dislocation loop under stress. The parallel dumbbells slid in the $\langle 111 \rangle$ direction under stress, resulting in the change of the habit plane of the dislocation loop. (b) The rotation of the habit plane under different stress levels with MS calculations. The straight arrow indicates the normal direction of the habit plane.

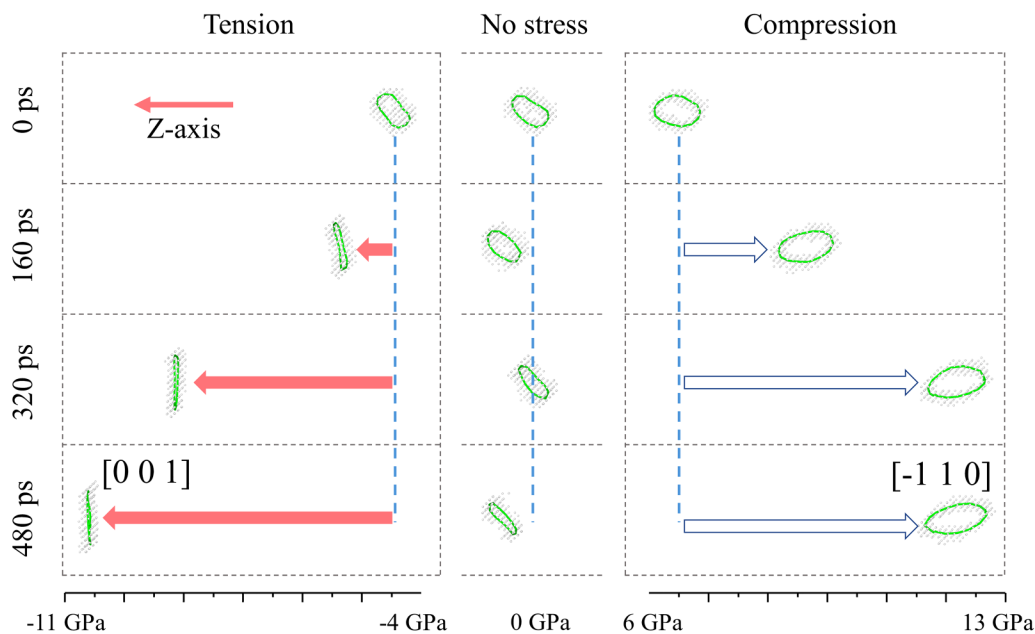


FIG. 8. Snapshots of the positions of the dislocation loop at different times under the tensile stress gradient, no stress, and compressive stress gradient field. The movement of the dislocation loop in the x- and y-directions was ignored, and the affine transformation method in OVITO was applied to avoid the dislocation loop being cut by the box boundaries.

the direction of the habit plane was affected by shear stress. This study showed that different stresses corresponded to different stable habit plane orientations. Figure 7(b) shows the normal direction of the habit plane under the effect of different strains; from the compressive to tensile states, the habit plane of the dislocation loop gradually changed from $\{110\}$ to $\{111\}$ and then to $\{001\}$.

Following the same method, the evolution of the dislocation loop in the stress gradient field was also simulated. Figure 8 shows the change in the habit plane orientation during the motion of the loop under the normal condition, compressive, and tensile stress gradient conditions. At the bottom of the figure, the approximate stress range where the dislocation loop passed was marked. Obviously, the stress on the left side of the box under the tensile stress gradient was the largest in the box, and the stress of the compressive stress gradient is concentrated on the right side of the box. From Fig. 8, we could infer that under the tensile stress gradient, the dislocation loop moved to the left of the box, and the habit plane gradually changes from $[\bar{1}11]$ to $[001]$. Under the compressive stress gradient, the dislocation loop moved to the right side of the box and the habit plane rotated to $[\bar{1}10]$. These behaviors agreed with the results of MS calculations in Fig. 7.

The results in Fig. 8 showed that the movement of the dislocation loop should be oriented as the dumbbell. Then, we simulated the movement of the dislocation loop under the compressive and tensile stress gradient fields several times. The dislocation loop moved along the negative z -direction under the compressive stress gradient, and along the positive z -direction under the tensile stress state. Eventually, the dislocation loop moved to the location of stress concentration in both states.

As shown in Fig. 8, comparing the position of the dislocation loop in the box at different times, the stress gradient field significantly accelerated the dislocation loop migration. The magnitude of the migration velocity of the dislocation loop in the three boxes

was of the order $V_{\text{compress}} > V_{\text{tensile}} > V_{\text{equilibrium}}$. The average diffusion coefficients of dislocation loops in the equilibrium field, stress field (box strain at -2%), and stress gradient field (at 3.15×10^{-2} GPa/Å with box stress range -12 to -4 GPa) at a temperature of 700 K were $5.17 \pm 0.94 \times 10^{-4}$, $5.02 \pm 1.14 \times 10^{-4}$, and $5.28 \pm 0.83 \times 10^{-3}$ Å²/fs, respectively. Since the diffusion coefficient under the stress gradient was an order of magnitude higher than the other two, it could be concluded that this acceleration effect was due to the stress gradient rather than the stress.

C. Simulations of a vacancy in W

The atomistic process of vacancy migration consisted of one atom next to the vacant site jumping into the site and leaving behind another vacant site. The self-diffusion coefficient determined the transport of atoms through the crystal under conditions near the thermodynamic equilibrium.⁴¹ Figure 9 shows the dependences of formation and migration energies of a single vacancy on the applied strain. The vacancy formation energy increased with strain (from compressive to tensile state), which was the opposite of the case of SIA. In the absence of strain, the formation energy of a single vacancy is 3.43 eV (DFT result was 3.56 eV¹²). Compared with the unstrained state, the variation in the vacancy formation energy was smaller than 0.2 eV, which was much smaller than that of SIA. From Fig. 9(b), the vacancy migration energy in the compressive and tensile stress field reduced by 0.05 eV with the stress value around 15 GPa compared with the value obtained in the equilibrium state. Therefore, comparing to the case of an SIA under the effect of strain field, slight changes of formation and migration energies induced by the strain field indicated that the external stress gradient might slightly affect vacancy migration. Considering the higher migration energy of a single vacancy, the

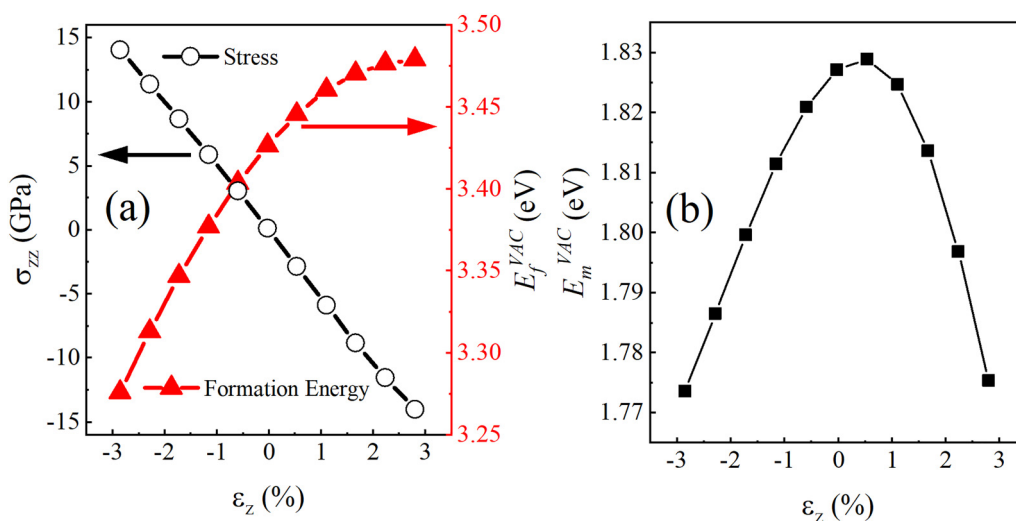


FIG. 9. (a) Formation energy (E_f^{vac}) of a vacancy at different strains in the z -direction, the stress-strain data of W are plotted with blue lines and circles. (b) Migration energy (E_m^{vac}) of one vacancy from one site to its nearest neighbor at different strain.

future study would be conducted using the accelerated MD method, which was not be presented in this study.

IV. CONCLUSIONS

The behaviors of some typical radiation-induced defects in W bulk under stress gradient fields were simulated with MS and MD methods. The dynamics simulations showed that SIAs have a tendency to migrate toward the stress concentration area in the stress gradient field. When the stress gradient increased, this tendency became more pronounced. In the static calculation of the dumbbell, the formation energy decreased and the migration energy increased when the stress state changed from compression to tension. Thus, the stress gradient caused an energy gradient inside W bulk, which led to the net movement of the dumbbells to the stress concentration area. Compared with the dumbbell, the influence of the stress gradient field on dislocation loops was more significant. Under the stress gradient field in W bulk, the normal vector of the habit plane of dislocation loops changed. When the stress state changed from compression to tension, the habit plane of the dislocation loop gradually changed from $\{110\}$ to $\{111\}$ and then to $\{001\}$. More importantly, the migration of dislocation loops was accelerated toward the stress concentration area in the stress gradient field. It could be inferred that the fast net movement will make those defects accumulate in a stress concentration area, which has a serious impact on service performance of the material. Thus, the stress gradient's impact on radiation defects should be considered in the design of PFMs.

ACKNOWLEDGMENTS

This work was financially supported by the National Natural Science Foundation of China (Nos. 12075141, 11375242, 51771073, and 11675230).

DATA AVAILABILITY

The data that support the findings of this study are available from the corresponding authors upon reasonable request.

REFERENCES

- ¹A. Hasegawa, T. Tanno, S. Nogami, and M. Satou, *J. Nucl. Mater.* **417**, 491 (2011).
- ²J. C. He, G. Y. Tang, A. Hasegawa, and K. Abe, *Nucl. Fusion* **46**, 877 (2006).
- ³A. Hasegawa, M. Fukuda, K. Yabuuchi, and S. Nogami, *J. Nucl. Mater.* **471**, 175 (2016).
- ⁴J. H. You and H. Bolt, *J. Nucl. Mater.* **299**, 9 (2001).
- ⁵K. Ioki, V. Barabash, A. Cardella, F. Elio, Y. Gohar, G. Janeschitz, G. Johnson, G. Kalinin, D. Lousteau, M. Onozuka, R. Parker, G. Sannazzaro, and R. Tivey, *J. Nucl. Mater.* **258–263**, 11 (1998).
- ⁶S. Timoshenko, "Theory of Elasticity" (McGraw-Hill, New York, 1970), p. 279.
- ⁷G. Janeschitz, *J. Nucl. Mater.* **290–293**, 1 (2001).
- ⁸S. Suzuki, Y. Ueda, K. Tokunaga, K. Sato, and M. Akiba, *Fusion Sci. Technol.* **44**, 41 (2003).
- ⁹H. Bolt, V. Barabash, W. Krauss, J. Linke, R. Neu, S. Suzuki, N. Yoshida, and ASDEX Upgrade Team, *J. Nucl. Mater.* **329–333**, 66 (2004).
- ¹⁰K.-D. Rasch, R. W. Siegel, and H. Schultz, *Philos. Mag. A* **41**, 91 (1980).
- ¹¹P. M. Derlet, D. Nguyen-Manh, and S. L. Dudarev, *Phys. Rev. B* **76**, 054107 (2007).
- ¹²D. Nguyen-Manh, A. P. Horsfield, and S. L. Dudarev, *Phys. Rev. B* **73**, 020101 (2006).
- ¹³K. Heinola and T. Ahlgren, *J. Appl. Phys.* **107**, 113531 (2010).
- ¹⁴M. Muzyk, D. Nguyen-Manh, K. J. Kurzydowski, N. L. Baluc, and S. L. Dudarev, *Phys. Rev. B* **84**, 104115 (2011).
- ¹⁵G. J. Ackland and R. Thetford, *Philos. Mag. A* **56**, 15 (1987).
- ¹⁶M. W. Finnis and J. E. Sinclair, *Philos. Mag. A* **50**, 45 (1984).
- ¹⁷N. Juslin and B. D. Wirth, *J. Nucl. Mater.* **432**, 61 (2013).
- ¹⁸D. Wang, N. Gao, Z. G. Wang, X. Gao, W. H. He, M. H. Cui, L. L. Pang, and Y. B. Zhu, *Nucl. Instrum. Methods Phys. Res. Sect. B* **384**, 68 (2016).
- ¹⁹V. V. Kirsanov, S. B. Kislitsin, and E. M. Kislitsina, *Phys. Status Solidi (A)* **86**, 199 (1984).
- ²⁰M. Li and R. L. B. Selinger, *Phys. Rev. B* **67**, 134108 (2003).
- ²¹Y. Chen, J. Fang, L. Liu, W. Hu, N. Gao, F. Gao, and H. Deng, *Comput. Mater. Sci.* **163**, 91 (2019).
- ²²Y. Chen, Y.-H. Li, N. Gao, H.-B. Zhou, W. Hu, G.-H. Lu, F. Gao, and H. Deng, *J. Nucl. Mater.* **502**, 141 (2018).
- ²³J. Fang, L. Liu, N. Gao, W. Hu, F. Gao, and H. Deng, *J. Appl. Phys.* **128**, 065103 (2020).
- ²⁴S. Plimpton, *J. Comput. Phys.* **117**, 1 (1995).
- ²⁵Y. Chen, J. Fang, L. Liu, W. Hu, C. Jiang, N. Gao, H.-B. Zhou, G.-H. Lu, F. Gao, and H. Deng, *J. Nucl. Mater.* **522**, 200 (2019).
- ²⁶M.-C. Marinica, L. Ventelon, M. R. Gilbert, L. Proville, S. L. Dudarev, J. Marian, G. Bencteux, and F. Willaime, *J. Phys.: Condens. Matter* **25**, 395502 (2013).
- ²⁷J. Fu, Y. Chen, J. Fang, N. Gao, W. Hu, C. Jiang, H.-B. Zhou, G.-H. Lu, F. Gao, and H. Deng, *J. Nucl. Mater.* **524**, 9 (2019).
- ²⁸L. Liu, Y. Chen, N. Gao, W. Hu, S. Xiao, F. Gao, and H. Deng, *Comput. Mater. Sci.* **173**, 109412 (2020).
- ²⁹F. Gao, H. Heinisch, and R. J. Kurtz, *J. Nucl. Mater.* **351**, 133 (2006).
- ³⁰C. S. Becquart and C. Domain, *Nucl. Instrum. Methods Phys. Res. Sect. B* **255**, 23 (2007).
- ³¹G. Bonny, D. Terentyev, A. Bakaev, P. Grigorev, and D. V. Neck, *Model. Simul. Mater. Sci. Eng.* **22**, 053001 (2014).
- ³²L. Ventelon, F. Willaime, C.-C. Fu, M. Heran, and I. Ginoux, *J. Nucl. Mater.* **425**, 16 (2012).
- ³³D. Wang, N. Gao, W. Setyawan, R. J. Kurtz, Z.-G. Wang, X. Gao, W.-H. He, and L.-L. Pang, *Chin. Phys. Lett.* **33**, 096102 (2016).
- ³⁴G. Henkelman, B. P. Uberuaga, and H. Jónsson, *J. Chem. Phys.* **113**, 9901 (2000).
- ³⁵W. Setyawan, G. Nandipati, and R. J. Kurtz, *J. Nucl. Mater.* **484**, 30 (2017).
- ³⁶A. Stukowski, *Model. Simul. Mater. Sci. Eng.* **18**, 015012 (2010).
- ³⁷W. H. Zhou, C. G. Zhang, Y. G. Li, and Z. Zeng, *J. Nucl. Mater.* **453**, 202 (2014).
- ³⁸J. Wang, B. He, W. Song, and W. Dang, *Mol. Simul.* **45**, 666 (2019).
- ³⁹D. R. Mason, X. Yi, M. A. Kirk, and S. L. Dudarev, *J. Phys.: Condens. Matter* **26**, 375701 (2014).
- ⁴⁰N. Gao, J. Chen, R. J. Kurtz, Z. G. Wang, R. F. Zhang, and F. Gao, *J. Phys.: Condens. Matter* **29**, 455301 (2017).
- ⁴¹W. G. Wolfer, in *Compr. Nucl. Mater.*, Second Ed, edited by R. J. M. Konings, and R. E. Stoller (Elsevier, Oxford, 2020), pp. 1–49.